Soft hydrogel-embedded ceramic skeleton mimicking bone structure via sacrificial bond concept

Sukamto[1], Milena Lama[2], Jian Ping Gong[2,3] Takayuki Nonoyama[3]*

[1]Graduate School of Life Science, Hokkaido University, Sapporo, 001-0021, Japan

[2]Institute for Chemical Reaction Design and Discovery (WPI-ICReDD), Hokkaido University, Sapporo, 001-0021, Japan

[3]Faculty of Advanced Life Science, Hokkaido University, Sapporo, 001-0021, Japan

Abstract

Bone, consisting of calcium phosphate minerals, rigid collagen fibrils, and acidic proteins, exhibits stiff and tough mechanical properties. On a molecular scale, covalent cross-linking in proteins, ionic interactions within proteins and at the protein-mineral boundary contribute to bone's toughness. In addition, hierarchical structures, like the sponge-like arrangement, are also crucial for the energy dissipation system in bone. Inspired by the multiple sacrificial bonds found in bone, we developed a soft/hard composite made up of two components with contrasting mechanical properties: a porous calcium phosphate skeleton and an acidic polymer hydrogel matrix. The porous ceramic skeleton alone is extremely rigid but brittle. However, the presence of the hydrogel matrix transforms the brittle nature of the porous ceramic skeleton into a soft/hard composite with stretchable and tough characteristics. The composite exhibits significant energy dissipation due to the fracture of the ceramic skeleton under small deformation, while catastrophic failure of the composite is prevented because the hybridized matrix disperses the damage throughout the entire sample. The Ca^{2+}-mediated ionic

bonding within the matrix hydrogel and at the boundary between the gel and skeleton effectively transfer the stress, enhancing the composite's toughness. Furthermore, the cyclic deformation generates new bare surfaces on the ceramic skeleton, leading to increased interaction between the matrix and these new surfaces, which enhances the composite's healing capability. This study demonstrates that the concept of multiple sacrificial bonds in bone is a smart strategy for designing polymer-ceramic composites with excellent mechanical properties.

Keyword: *Hydrogel, soft/hard composite, sacrificial bond concept, porous ceramic skeleton, bone mimicking*

1. Introduction

Mammalian bones and teeth are stiff and tough, enabling us to engage in physical activity and chew hard foods. They consist of hierarchical tissues composed of calcium phosphate (CaP) mineral hydroxyapatite (HAp), type I collagen, acidic non-collagenous proteins (NCPs) such as osteopontin (OPN) and osteocalcin, and a small amount of water [1-2]. On a molecular scale, triple-helical collagen forms a relatively stiff framework that serves as a platform for HAp biomineralization. In this environment, acidic NCPs interact with HAp-mineralized collagen fibrils through calcium-mediated bonding [3]. Additionally, OPN molecules form intra- and intermolecular covalent cross-links with each other via enzymatic reactions [4]. The coexistence of static and dynamic cross-link structures contributes to the toughness of bone tissue at the molecular level. When an impact occurs, the covalent cross-links efficiently transfer the force to the non-covalent cross-linking structures, which can dissipate energy through the dissociation of ionic bonds. This type of bond structure, which preferentially breaks to prevent catastrophic fracture, is known as a “sacrificial bond” [5]. It has been suggested that the synergistic effect of static and dynamic bond structures contributes to the stiff yet tough nature of bones. Recently, inspired by the molecular structure of bone, a

material combining acidic polyacrylic acid (PAAc) hydrogel with HAp particles has been reported to replicate a similar co-crosslinking structure, resulting in tunable and excellent mechanical properties [6].

Moreover, not only the molecular-scale structure but also the hierarchical porous structure of spongy bone contributes to the mechanical properties of bone. At the macroscopic level, bone can be primarily categorized into two types: compact bone (cortical bone) and spongy bone (trabecular bone). Compact bone forms the dense outer shell of the bone structure, with a relatively low porosity of 5-10% and a high apparent density of 1.5-1.8 g/cm³. In contrast, spongy bone is composed of a porous framework of thin, column-like structures called trabeculae. This open-cell, lattice structure gives trabecular bone a high surface area to mass ratio, allowing it to deform elastically under load and dissipate energy through the bending of trabeculae. The trabeculaes in spongy bone are also aligned with the direction of applied force, further enhancing the bone's mechanical performance [7-9]. Spongy bone has a much higher porosity, ranging from 50-90%, and a lower apparent density of 0.5-1.0 g/cm³. The distinct porous structures of compact and spongy bone contribute to their different mechanical properties. The dense, compact bone provides high mechanical strength, while the porous spongy bone offers elasticity and helps dissipate mechanical energy [10-12].

In this study, we present a concept for developing a tough and soft composite material inspired by the molecular and hierarchical structures of bone. The material consists of a brittle, porous biphasic calcium phosphate (BCP) skeleton as the hard ceramic component and a poly(acrylic acid) (PAAc) cross-linked hydrogel matrix containing carboxyl groups, which simulate the role of non-collagenous proteins in bone. This approach does not attempt to replicate bone itself while emulates bone's intrinsic toughening mechanisms through multiple

sacrificial bonds (**Fig. 1**), with a focus on enhancing the mechanical properties of synthetic soft materials.

The porous BCP ceramic skeleton, characterized by an extensive surface area, is prepared using a simple sponge templating method that replicates the structure of a conventional urethane sponge through sintering of the HAp slurry-coated sponge [13-15]. HAp was selected as the initial slurry material because, during sintering, it partially transforms into β-TCP, resulting in a BCP ceramic skeleton containing both HAp and β-TCP phases. This biphasic structure leverages the complementary properties of the two phases. The β-TCP phase facilitates a controlled release of calcium ions to promote cross-linking, while the HAp phase preserves the structural integrity and mechanical strength of the skeleton due to its mild dissolution behavior in acidic conditions. When the acidic PAAc hydrogel is synthesized with a chemical cross-linker in the presence of the BCP ceramic skeleton, the hydrogel occupies the entire pore space, achieving full integration with the skeleton. Simultaneously, calcium ions are partially eluted from the ceramic skeleton under acidic conditions. This process enables the PAAc gel matrix to form calcium-mediated cross-links alongside covalent cross-link structures, mimicking the role of osteopontin (OPN) in bone. Dynamic ionic interactions at the interface between the calcium ions on the skeleton's surface and the carboxyl groups in the gel enhance interfacial adhesion, facilitating efficient force transfer between the hard sponge and the soft matrix.

Unlike conventional composites made from hydroxyapatite (HAp) powder and acidic hydrogel, the ceramic skeleton in our design possesses a continuous structure. This feature is expected to provide additional energy dissipation through the fracture of the skeleton under deformation. The hydrogel matrix prevents catastrophic fracture of the ceramic skeleton by dispersing damage throughout the composite via force transfer. Furthermore, when local

fractures occur in the porous ceramic skeleton, new surfaces are exposed, which are expected to form additional interactions with the PAAc hydrogel during annealing.

The expected toughness mechanism of this composite material, which combines a hard phase with a soft phase based on the sacrificial structure, relies on principles commonly found in tough soft materials, with double network (DN) hydrogels being a representative example [16]. DN gels consist of two contrasting polymer networks: the "first network" is relatively hard and brittle due to nearly fully stretched polymer strands (the “hard phase”), while the "second network," which is more concentrated, consists of relatively relaxed and flexible polymer chains (the “soft phase”). The enhanced toughening mechanism of DN gels has been attributed to two main effects. Firstly, when the material is deformed or stretched, the covalent bonds in the stiff first network break, dissipating energy. Simultaneously, the flexible second network maintains the overall integrity of the material, preventing it from completely falling apart [17]. Similarly, in the composite material, the BCP skeleton with its sponge-like structure is designed to fracture under deformation, dissipating energy, while the soft polymer matrix allows the composite to deform and prevents catastrophic failure.

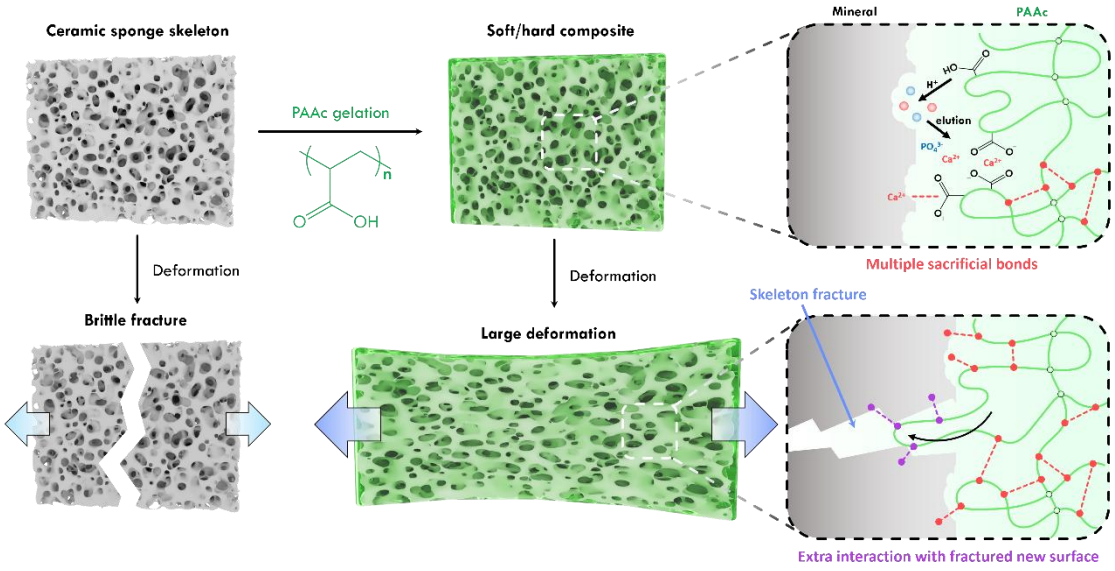

Fig. 1 Concept of a tough composite material consisting of a hard CaP ceramic sponge skeleton and a soft, acidic polymer cross-linked hydrogel with multiple sacrificial structures. When the PAAc hydrogel is hybridized with the CaP ceramic sponge skeleton, ionic interactions occur between the calcium ions on the CaP surface and the carboxyl groups of the PAAc. In molecular scale, the green circles indicate points of covalent cross-linking. In the acidic environment, the CaP partially dissolves, and the eluted calcium ions form ionic cross-links with the PAAc polymer network. During deformation of the soft/hard composite, the sacrificial fracture of the skeleton dissipates energy. Additionally, extra interactions (indicated by purple dashed lines) between the PAAc and the fractured CaP surface form during annealing.

2. Experimental section

2.1. Material

Hydroxyapatite (HAp) powder (purum p.a., ≥90% as $Ca_3(PO_4)_2$, KT), polyvinyl alcohol (PVA) binder with a 2000 DP, acrylic acid (AAc), acrylamide (AAm) monomers, N,N′-methylenebisacrylamide (MBAA) crosslinker, and potassium peroxodisulfate (KPS) initiator were purchased from Sigma-Aldrich Co. LLC, US. POIZ 520 dispersant, containing sodium polyacrylate, was purchased from Kao Corporation, Japan. All chemicals were used as received. Two kinds of commercially available urethane sponges, Scotch-Brite® (S-21KS) and PAX NATURON (124365), were purchased from 3M Company, US, and Taiyo Yushi Corporation, Japan, respectively. The distilled water used in all experiments was supplied by a Milli-Q® water system (Integral 5, Merck Millipore, US).

2-2. Soft/hard composite fabrication

The plate-shaped soft/hard composite was fabricated by combining S1 and S2 ceramic sponges with a PAAc hydrogel matrix. The ceramics S1 and S2 were prepared using a coating process, and the detailed procedure is provided in the **Supporting Material**. The precursor solution for the poly(acrylic acid) (PAAc) matrix was prepared using 3 to 7 M AAc monomer, 0.1 mol% MBAA as a covalent bond cross-linker, and 0.1 mol% KPS as an initiator. The mol% of the cross-linker and initiator was calculated relative to the concentration of the monomer. The sintered ceramic sponge, immersed in the precursor solution, was placed in a mold made of a silicone spacer with a thickness of 5 mm. This mold was sandwiched between two glass plates and subjected to thermal polymerization at 80 °C for 8 hours. As control samples, soft/hard composites with a neutral PAAm gel matrix were prepared in the same manner.

2-3. Thermogravimetric analysis

The thermal stability of the materials was determined using thermogravimetric differential thermal analysis (TG-DTA, Thermoplus Evo TG 8120, Rigaku, Japan). The soft/hard composite samples were placed in a platinum pan and heated from room temperature to 700 °C at a rate of 10 °C/min under a constant flow of nitrogen gas.

2-4. Observation of morphology

Morphological analysis was performed using a scanning electron microscope (JSM-6010LA, JEOL, Japan). The soft/hard composites were cut, and the cross-sectional surface was selected for observation. The samples were mounted on a brass sample plate with double-sided carbon tape. To enhance the samples' electroconductivity, Pd/Au ion sputtering was applied using an E-1010 ion sputter system (Hitachi, Japan). The acceleration voltage was set to 15 kV.

158 Pore size measurements were carried out using ImageJ software, with calculations for coarse,
159 intermediate, and fine pores. The determination of pore size involved a series of steps to account
160 for the irregular shape of the fine pores. The pore size measurements were conducted using
161 more than three SEM images of each skeleton to ensure accuracy and reliability of the data.
162 Additionally, elemental mapping was performed using energy-dispersive X-ray spectroscopy
163 (EDX) installed in the SEM.
164
165 **2-5. Mechanical testing**
166 Mechanical properties of the porous ceramic skeletons, and as prepared soft/hard
167 composites were evaluated at room temperature using a mechanical tester (Shimadzu AGX-V,
168 Shimadzu Co., Japan).
169 Uniaxial compressive testing was conducted on the porous ceramic skeleton at a
170 velocity of 1 mm/min. The samples had specific dimensions (15 × 15 × 15 mm^3), and each test
171 was performed on three samples. The global Young's modulus was determined by linear fitting
172 in the linear region of the stress-strain curve [18].
173 Uniaxial tensile deformation was applied to both the soft/hard composite and its
174 components, including the hydrogel matrices and the porous ceramic skeleton. The samples had
175 specific dimensions (20 × 10 × 5 mm^3). All samples were stretched along the length direction
176 at a velocity of 10 mm/min, with each test performed on five samples.
177 Cyclic loading and unloading tensile tests were conducted on the soft/hard composite.
178 All samples, with same dimensions with the tensile sample, were stretched to a strain of 2
179 mm/mm at a velocity of 100 mm/min with varying waiting times (0, 1, 10, 30, and 60 min).
180 Subsequently, the samples were returned directly to the initial strain at the same rate as
181 stretching.

To evaluate the adhesion energy between the biphasic calcium phosphate (BCP) bulk plate and the hydrogel matrix, a 90° peeling test was conducted. The BCP bulk plate, with dimensions of 20 × 20 × 30 mm^3, was prepared using the HAp slurry with the same formulation as the ceramic skeleton fabrication, excluding the sponge template. The PAAc gel, prepared from 4 M AAc, 0.1 mol% MBAA, and 0.1 mol% KPS, was polymerized directly onto the HAp plate, with half of the surface covered with an anti-adhesive sheet to prevent adhesion. The uncoated part of the hydrogel was clamped by an upper jig connected to a 100 N load cell. To prevent elongation of the clamped gel handles, the surface of the gel was reinforced with cloth tape (Nichiban Co., Ltd., Japan). As-prepared samples without swelling in water were used. As a control, polyacrylamide (PAAm) gel was prepared on the BCP plate in the same manner. The peeling test was conducted at a pulling speed of 100 mm/min. The adhesion energy was determined using the formula $g=\frac{F_{ave}}{w}$, where F_{ave} represents the average force at the plateau in the steady-state region of the peeling process. For samples that did not reach the steady state, the force at the fracture point was used. The w denotes the width of the test hydrogel sheet.

3. Result and discussion

3-1 Optimization of the ceramic skeleton's formulation as a rigid sponge skeleton

We initially fabricated rigid sponge skeletons from HAp precursor slurry to serve as the sacrificial-bond structure using the sponge template method. Two commercial urethane sponges with different architectures including pore size and strut length were utilized (**Fig.2A and 2B**): a sponge template with an average pore size of 760 μm and strut length of 540 μm (designated as S1) and another with average pore size of 620 μm and strut length of 352 μm designated as S2) (**Fig. S1**). The morphology of the porous ceramic skeletons provided by the sintering urethane sponge template coated by HAp slurry, 50wt% HAp powder and 20wt% and 15wt%

of PVA for S1 and S2, is illustrated in **Fig. 2C and 2D**. As expected, the S1 pore structure exhibits larger pore sizes compared to the S2 pore structure. Interestingly, the ceramic skeletons exhibit not only coarse pores originating from the urethane sponge structure, but also intermediate and fine pores formed during the combustion of the sponge template. Additionally, fine pores were created as spaces between ceramic particles after the sintering process. For the S1 skeleton, coarse and intermediate pore sizes ranged between 720±307 μm and 101±71 μm, respectively, while for the S2 skeleton, these values were 540±253 μm and 46±33 μm. The fine pore sizes for both skeletons ranged between 34 to 365 nm. The pore size measurements and representative SEM images for each skeleton are provided in **Fig. S2 and S3**.

According to SEM images and pore size analysis, the pore distribution in the S2 skeleton is more regular compared to the S1 skeleton. This difference can be attributed to the longer struts of the S1 sponge template, which lead to a more irregular pore structure in the resulting ceramic skeleton after the combustion process. The uniformity of pore distribution was further evaluated by comparing the standard deviation of pore sizes, with the S2 skeleton showing a lower standard deviation, confirming its more homogeneous structure.

Traditionally, HAp sintering has been carried out at high temperatures exceeding 1300 ºC, which often results in excessive densification and decreasing porosity due to grain-melting fusion. In this study, we employed the sintering condition at 1000 ºC for the fabrication of brittle porous ceramic skeleton. At this temperature, the HAp particles do not undergo complete melting and merging, maintaining nanocrystalline grain structure. It ensures the rigid and fragile nature of the ceramic skeleton with extraordinary high surface area. This rigidity is a desirable characteristic for the skeleton to act as a sacrificial structure on the further soft/hard composite. The high surface area will take efficient interfacial interaction with soft matrix when hybridized.

The obtained ceramic sponge skeleton is relevant to previous works on fabricating porous ceramic using a sponge template, where the size of pores ranges from 200 to 700 μm, which is similar to the structure of the sponge template [19]. The coarse pore size of this material closely resembles that of real trabecular bone, which typically falls within the range of 300-500 μm [20]. The ceramic sponge has extraordinarily high surface area due to the hieratical pore structure, expecting that when the CaP sponge and acidic hydrogel are hybridized, the hydrogel matrix will occupy every scale of pore and form numerous numbers of interfacial interaction at the boundary.

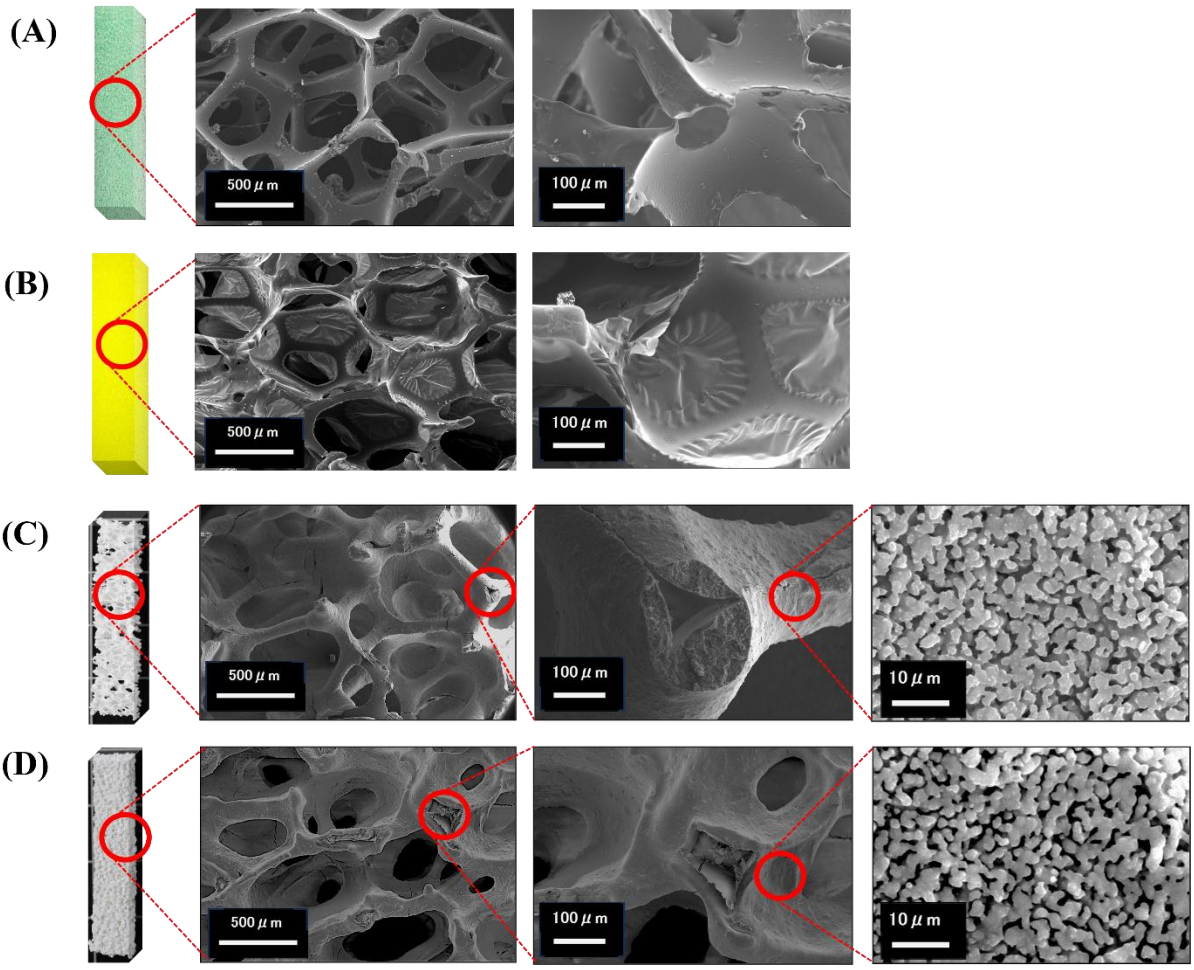

Fig. 2 Morphology and pore structure of S1 (A) and S2 (B) urethane sponges and sintered ceramic skeletons from S1 (C) and S2 (D).

The mechanical properties of the sintered ceramic skeleton can be adjusted by altering the slurry composition. To optimize these properties, we prepared skeletons with varying ratios of PVA binder and HAp powder. The mechanical properties of the porous ceramic skeleton were evaluated using a compressive test (**Fig. S4**). Due to the porous structure, the nominal stress of the skeletons was calculated by dividing the applied force by the macroscopic top-surface area of the porous skeleton samples. **Fig. 3A and 3B** illustrate the compressive strength and Young's modulus at different PVA concentrations, with a fixed 50wt% HAp powder ratio. The two ceramic skeletons, S1 and S2, exhibit distinct fracture behaviors. The S1 ceramic skeleton shows a lower stress increase compared to the S2 skeleton. The S1 template has a larger pore size, longer strut length, and fewer struts compared to the S2 template. As a result, the S1 template is more prone to fracture initiation at the junctions where the struts meet due to increased localized stress in these areas. Additionally, longer struts are more likely to contain defects along their length, which can serve as weak points for crack propagation. Moreover, the occurrence of grain separation at the borders of the long struts contributes to the formation of a zig-zag fracture profile. In contrast, the S2 skeleton with 20wt% PVA also displays a zig-zag fracture pattern, although the struts are much smaller than those in S1. The greater number of struts in S2 ensures that even if one strut fails, the overall structure is minimally affected, as many additional struts continue to support the load. However, the distinct zig-zag profile is also observed in the S2 sample with 20wt% PVA, which closely resembles that of the S1 sample. The increase in PVA binder concentration leads to an increase in slurry viscosity, making it difficult for the slurry to penetrate the sponge template and form thinner struts. This results in the sintered skeleton having more intrinsic defects than those prepared with lower PVA concentrations. On the other hand, when the sponge is coated with low-viscosity slurry containing a low PVA concentration, the HAp powder tends to drip off easily, making it

265 difficult to remain on the sponge. Increasing the ratio of HAp powder also increases the slurry
266 viscosity [21]. As shown in Figure 3, adding 20wt% PVA binder to the S1 skeleton and 15wt%
267 to the S2 skeleton resulted in maximum compressive strengths of 36±3.9 kPa and 51±7.8 kPa,
268 respectively. Furthermore, when the HAp fraction was varied from 50 to 60wt%, the 50wt%
269 ratio produced ceramic skeletons with the highest mechanical strength (**Fig. S4**). In summary,
270 the optimal conditions for the S1 and S2 porous ceramic skeletons were achieved by
271 incorporating 15wt% and 20wt% PVA, respectively, into a 50wt% HAp powder ratio. The
272 Young's modulus of the S2 skeleton is 7.44±0.085 MPa, which is double that of the S1 skeleton,
273 at 3.79±0.015 MPa. These ceramic skeletons with the highest mechanical strength were selected
274 for combination with the hydrogel matrix to create the soft/hard composite.

275 To evaluate the effect of the sintering process on the ceramic phase transition, we
276 analyzed the porous ceramic skeleton under optimal conditions using XRD **(Fig. 3C and 3D**).
277 According to the XRD diffractograms, the HAp slurry coated on the sponge templates
278 underwent a phase transition into BCP ceramic, consisting of HAp and beta-tricalcium
279 phosphate (β-TCP), due to the partial dissociation of HAp [22] after sintering at 1000 °C. As
280 observed in the XRD pattern, there is a sharp peak at $2\theta = 31.2^{o}$, which is characteristic of β-
281 TCP [23]. The formation of β-TCP as a result of the partial dissociation of HAp has a positive
282 effect on the dissolution ability of the ceramic skeleton in acidic conditions because β-TCP is
283 more soluble than HAp under such conditions. As mentioned in previous work, the presence of
284 the more soluble β-TCP phase in BCP makes the overall material more readily dissolvable
285 compared to pure sintered HAp [24]. This implies that Ca^{2+} ions in the ceramic skeleton will
286 dissolve more easily when combined with an acidic matrix hydrogel.

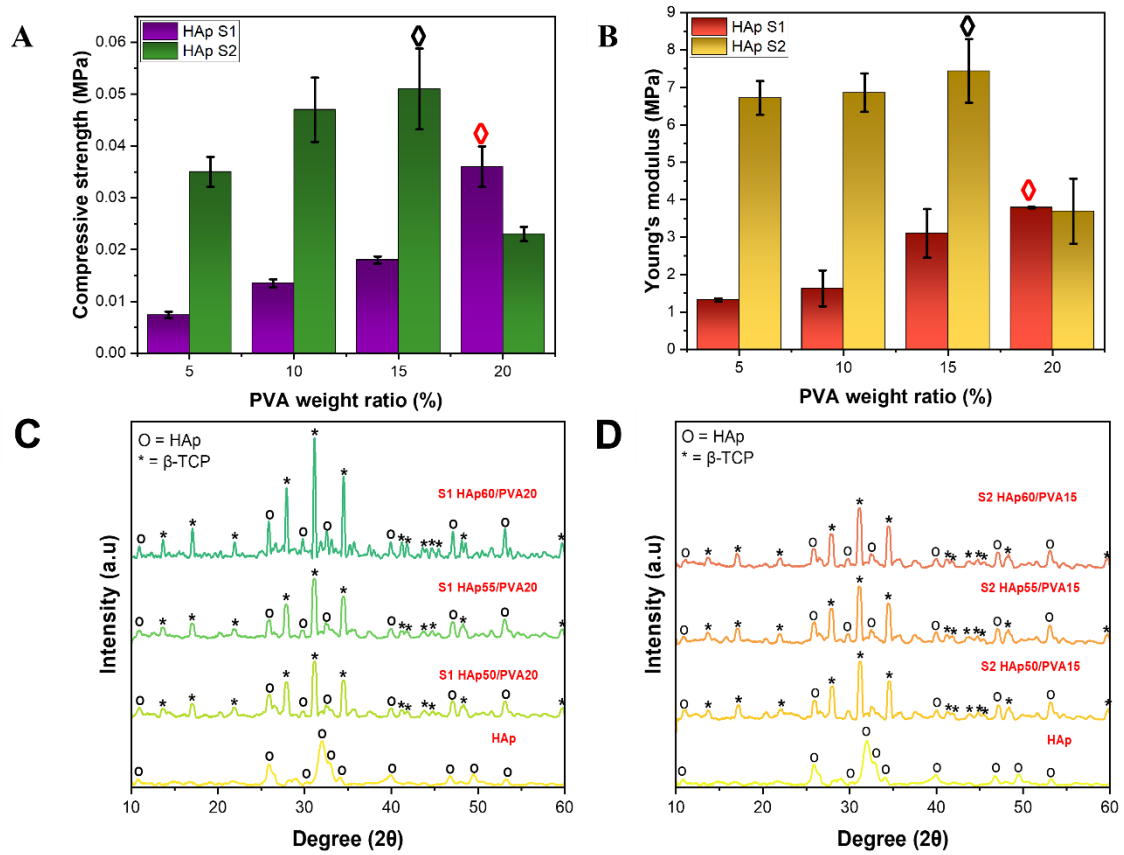

Fig. 3 (A) Compressive strength of S1 and S2 at different PVA ratio at 50 wt% HAp powder. (B) Young's modulus of S1 and S2 at different PVA ratio at 50 wt% HAp powder. ◊ Indicating the optimum concentration of PVA binder for each skeleton. XRD diffractogram of (C) S1 and (D) S2 at optimum PVA binder ratio. The bottom HAp is profile of raw HAp powder before sintering.

3-2 Structure of soft/hard composite and the effect of interfacial interaction

In the molecular structure of bones, acidic macromolecules like OPN form ionic interactions with the outermost surface of calcium phosphate minerals, contributing to bone toughness. Similarly, the ionic interfacial interaction between the ceramic skeleton and the hydrogel matrix is crucial for efficiently transferring forces between them during deformation. Previous investigations using photoacoustic Fourier transform infrared spectroscopy (FTIR-PAS) and molecular dynamics simulation (MDS) have provided insights into the role of interfacial interactions in the mechanical properties of HAp/PAAc composites [25]. These

studies have shown that the most favorable attachment of ionized polyacrylic acid (PAAc) occurs along the HAp surface, which has the highest density of calcium ions. The distance between the calcium ions and the oxygen atoms of the -COO^- groups in the ionized PAAc suggests the possibility of various types of chelation between the calcium ions and the -COO^- groups [26]. The interaction mechanism of PAAc with β-TCP is fundamentally similar to that with HAp due to the involvement of calcium ions and chelation [27].

To quantitatively evaluate this interaction, we conducted a 90° peeling test to calculate the adhesion energy between the PAAc hydrogel matrix and the BCP non-porous bulk plate, which was prepared using the same method as the ceramic skeleton fabrication. To reveal the effectiveness of the acidic moiety of PAAc, we also prepared a neutral poly(acrylamide) (PAAm) gel with an amide moiety as a reference. The PAAc hydrogel exhibits elongation during the peeling test, as indicated by the middle figure of **Fig. 4A** (red square). This elongation suggests that a higher force is required to peel the PAAc hydrogel from the BCP plate. On the other hand, the PAAm hydrogel in **Fig. 4B** shows no elongation, indicating it is easier to peel off due to weaker interactions with the BCP plate. The adhesion energy for the PAAc hydrogel against the BCP bulk surface was 105.7 J/m². In contrast, the neutral PAAm hydrogel showed significantly lower adhesion energy (38.29 J/m²), as shown in **Fig. 4C**. This confirms that the stronger interaction between the PAAc and BCP plate is due to calcium-mediated ionic bonding between the PAAc gel and the ceramic skeleton, which contributes to efficient load transfer during deformation.

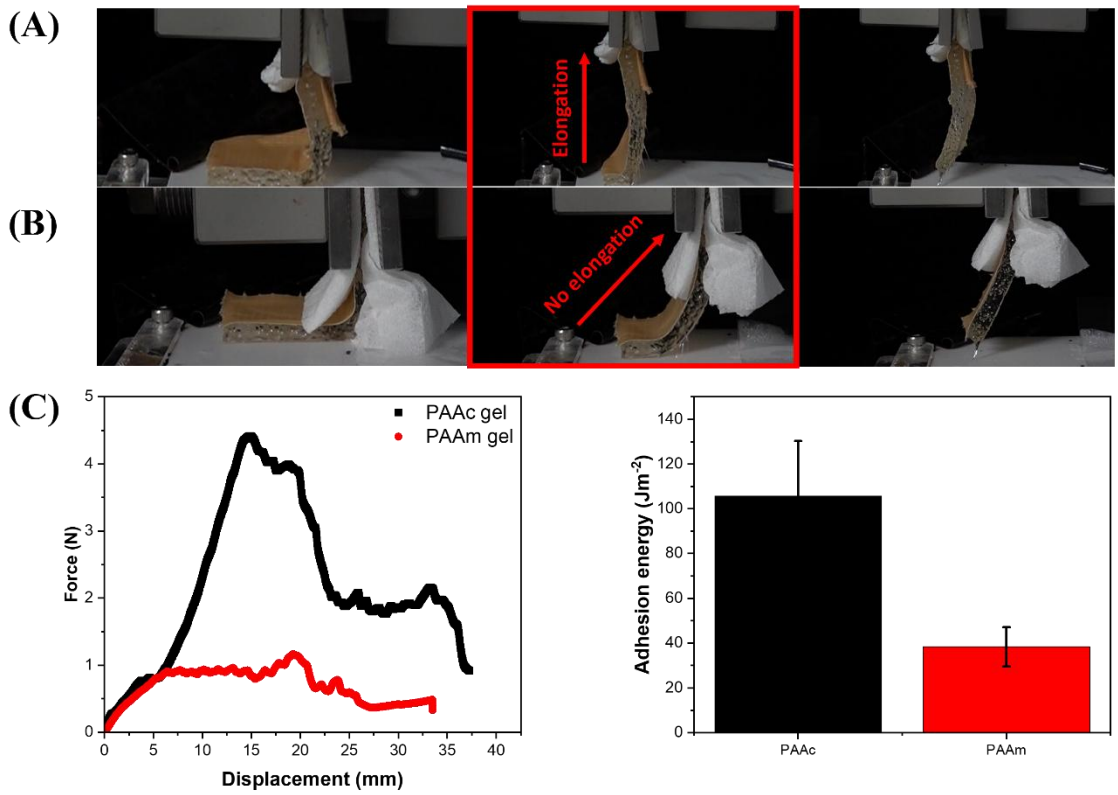

Fig. 4 Peeling test of (A) PAAc gel and (B) PAAm gel on the BCP plate. (C) Peeling force-displacement curves. (D) Adhesion energy between hydrogel and BCP plate.

To synthesize the soft/hard composite, we combined the S1 porous ceramic skeleton with a hydrogel matrix using thermal polymerization. To evaluate the effect of interfacial interactions, we used 4 M AAc as an anionic monomer with 0.1 mol% cross-linker, which can interact with the CaP ceramic skeleton, and AAm as a neutral monomer for comparison. During polymerization, the monomer solution not only filled the surface and coarse pores of the porous ceramic skeleton but also diffused into the intermediate and fine pores, occupying all the pore structures of the ceramic skeleton.

Fig. 5A shows the appearance of the soft/hard composite consisting of the S1 ceramic skeleton and the PAAc gel matrix. The gel hybridized with the ceramic skeleton without any

structural mismatch. SEM-EDX elemental analysis confirmed that the sintered ceramic sponge skeleton did not show any carbon, indicating complete combustion of the urethane sponge, whereas carbon was detected in the composite at both the primary coarse pores and the strut regions of the skeleton. This indicates that the entire pore system of the porous ceramic skeleton was completely filled by the hydrogel matrix (**Fig. 5B**). Similarly, the PAAm gel was also formed throughout the skeleton's pore structures, fully integrating with it (**Fig. S5**).

Moreover, when the PAAc hydrogel matrix was combined with the ceramic skeleton, calcium was detected in the hydrogel-filled coarse pore regions. It is well known that calcium phosphate salts can dissolve in acidic conditions. The dissociation of -COOH groups on the PAAc generates H^+ ions, which partially dissolve the ceramic skeleton, releasing calcium and phosphate ions into the PAAc hydrogel matrix [28]. This elution is crucial for enhancing the mechanical properties of the PAAc matrix by forming calcium-mediated ionic cross-links, similar to the role of OPN protein. The FT-IR spectrum of the PAAc-S1 composite shows a significant increase in the peak at 1550 cm^{-1} ($-COO^-$ asymmetric stretching) compared to that of the PAAc gel (**Fig. S6**), supporting the formation of calcium-mediated ionic cross-linking. Although calcium was also present in the PAAm system, its concentration was noticeably lower than in the PAAc system (**Fig. S7**).

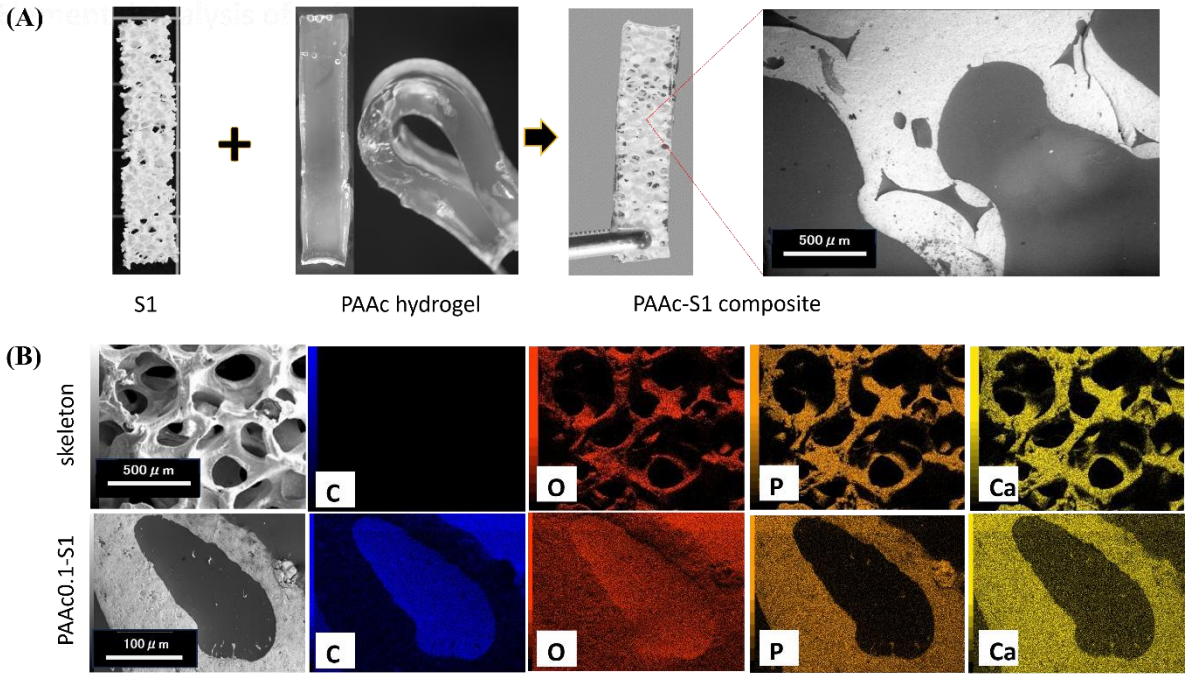

Fig. 5 (A) Appearance of S1 ceramic skeleton, PAAc hydrogel and PAAc0.1-S1 composite. The 0.1 denotes crosslinker concentration in mol%. (B) EDX elemental mapping of S1 ceramic skeleton and PAAc0.1-S1 composite.

The presence of the hydrogel matrix within the hierarchical structure of the skeleton significantly influences the mechanical interlocking between the ceramic skeleton and the hydrogel matrix. The interconnected pore structure of the skeleton increases the surface area available for interaction with the hydrogel matrix. This is supported by previous research, which demonstrates that the structure of porous fillers plays a crucial role in the micromechanical interlocking between fillers and resin, thereby enhancing the properties of dental resin composites [29]. Moreover, not only physical interlocking but also chemical interfacial interactions between the negatively charged hydrogel matrix and the ceramic skeleton are important for enhancing the mechanical properties of the material [30].

Fig. 6 presents the tensile profile and mechanical properties of PAAc-S1 and PAAm-S1 composites across various monomer concentrations. The PAAc-S1 composite demonstrates

superior stretchability compared to the neat ceramic skeleton, with multiple local fractures occurring before global failure (**Fig. 6C**). This is due to the strong interaction between the negatively charged carboxylic groups in the PAAc hydrogel and the positively charged calcium ions on the ceramic skeleton's surface. These robust interfacial interactions enhance load transfer between the hard ceramic skeleton and the soft gel matrix, thereby improving the composite's toughness. An increase in AAc monomer concentration further boosts the toughness of the PAAc-S1 composite, highlighting the critical role of interfacial interactions in optimizing composite performance [31]. In contrast, the neutral PAAm-S1 composites, although having the same swelling ratio as PAAc-S1, exhibit relatively lower toughness and only a single catastrophic fracture (**Fig. 6D**).

As shown in **Fig. 6E**, the fracture strength of both PAAc-S1 and PAAm-S1 composites increases with higher monomer concentrations. However, PAAc-S1 consistently exhibits higher fracture strength than PAAm-S1. This is attributed to the strong ionic bonding between the PAAc matrix and calcium ions in the ceramic skeleton, which enhances load transfer and reinforces the composite structure. In comparison, while PAAm-S1 also shows increased strength with higher monomer concentration, it lacks the reinforcing ionic interactions found in PAAc-S1. The hydrogen bonds in PAAm are weaker than the ionic bonds in PAAc, resulting in lower fracture strength for the PAAm-S1 composite.

The Young's modulus of both PAAc-S1 and PAAm-S1 composites also increases with higher monomer concentrations, reflecting enhanced stiffness (**Fig. 6F**). PAAm-S1 consistently exhibits a higher Young's modulus than PAAc-S1 due to the different nature of their polymer networks. In PAAm-S1, the absence of ionic interactions with calcium ions means that the polymer matrix relies on hydrogen bonding, which creates a denser and stiffer structure. This increased stiffness results in a higher Young's modulus for PAAm-S1. Conversely, the PAAc-

S1 composite benefits from ionic crosslinking between carboxyl groups (-COO^-) and Ca^{2+} ions. These ionic interactions introduce flexibility into the polymer network, leading to a lower Young's modulus compared to PAAm-S1. Despite the increased polymer entanglement with higher monomer concentrations in both materials, the ionic crosslinks in PAAc-S1 provide greater flexibility, resulting in a relatively lower modulus.

Fig. 6G illustrates that the work of extension, which measures the energy absorbed before fracture, increases significantly for PAAc-S1 composites as the monomer concentration rises. For example, increasing the AAc monomer concentration from 3 to 6 M raises the work of extension for PAAc-S1 from 401.47 to 696.17 kJ/m^3. This increase is due to the enhanced toughness provided by the ionic interactions between carboxyl groups and Ca^{2+} ions, which improve load transfer and energy absorption. In contrast, PAAm-S1 shows a less pronounced increase in work of extension due to the absence of ionic interactions, resulting in lower toughness despite a similar swelling ratio.

The fracture strain of both PAAc-S1 and PAAm-S1 composites decreases with higher monomer concentrations, as shown in **Fig. 6H**. This decrease is attributed to increased polymer entanglement, which restricts the mobility of the polymer chains and leads to greater stiffness and strength. While PAAc-S1 retains greater elongation at break compared to PAAm-S1, the denser polymer network resulting from higher monomer concentrations contributes to the observed reduction in fracture strain for both composites.

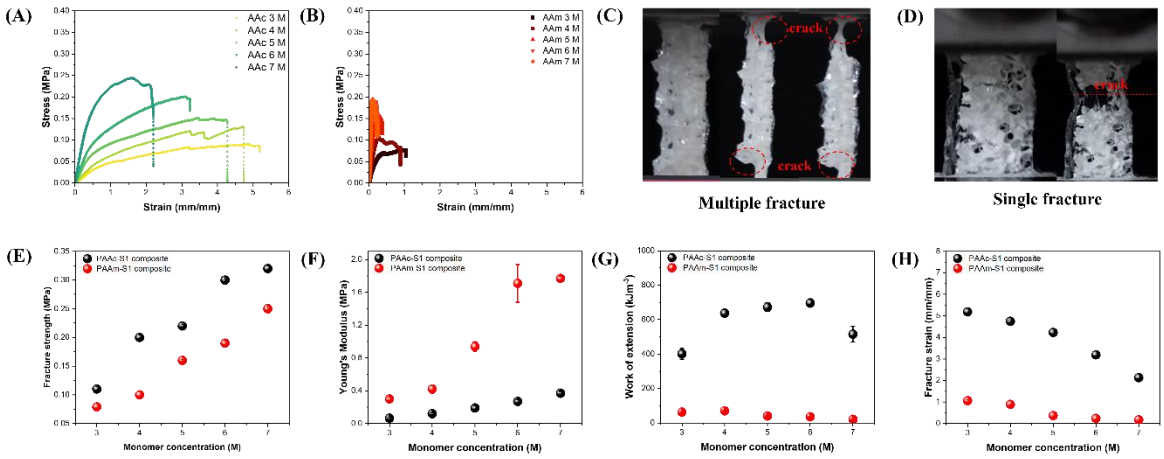

Fig. 6 Tensile mechanical profiles of the soft/hard composites. Stress-strain curves of (A) PAAc-S1 composites and (B) PAAm-S1 composites. Fracture profile of (C) PAAc-S1 composite and (D) PAAm-S1 composite. (E) Fracture strength of PAAc-S1 and PAAm-S1 composites. (F) Young's modulus of PAAc-S1 and PAAm-S1 composites. (G) Work of extension of PAAc-S1 and PAAm-S1 composites. (H) Fracture strain of PAAc-S1 and PAAm-S1 composites.

Moreover, it is important to note that the PAAc gel matrix itself is reinforced by calcium-mediated ionic cross-linking, as shown in **Fig. 5B and S7**. Calcium ions can form bridging interactions with the negatively charged carboxylic acid groups of the PAAc matrix through electrostatic interaction [32-33]. As mentioned in previous work [6], the PAAc-HAp composite system possesses a self-regulating feature due to the dual buffer effect of PAAc and calcium phosphate. Even though the initial state of the composite with calcium phosphate and acidic PAAc polymer varies based on different feed compositions, the final equilibrium state converges to a similar condition. During this process, calcium-mediated ionic bonds spontaneously form between the PAAc polymers, as well as between the polymer and minerals. Consequently, even with the same polymer concentration, the PAAc matrix is much stronger and tougher than the PAAm matrix in the composite.

To reveal the contribution of the ceramic sponge structure to the mechanical properties of the composite, we compared the PAAc-S1 composite with the PAAc-particulate HAp composite under cyclic tensile testing. The PAAc-particulate HAp composite was prepared using 4 M AAc monomer, 0.1 mol% MBAA crosslinker, and 10 vol% HAp powder, similar to the fabrication of the ceramic sponge. As a result, the HAp particles were not interconnected but were homogeneously distributed within the gel matrix. Based on the cyclic tensile curves of both composites with the same AAc concentration, the PAAc-particulate HAp composite exhibited lower hysteresis (50.56 kJ/m^3) compared to the PAAc-S1 composite (91.78 kJ/m^3) (**Fig. S8**). Assuming that energy dissipation from calcium-mediated ionic cross-linking at the mineral-polymer and polymer-polymer interfaces is comparable between the PAAc-particulate HAp composite and the PAAc-S1 composite, the energy dissipation due to the fracture of the ceramic skeleton structure is almost half of the total hysteresis (41.22 kJ/m^3). This result indicates that the skeleton structure of the ceramics greatly contributes to the toughness of the composite and efficiently dissipates energy at low strain due to the brittle nature of the sintered ceramics.

As mentioned above, in addition to the calcium-mediated ionic bonds present between the PAAc chains and the skeleton as well as between the PAAc chains themselves, the fracturing of the ceramic skeleton generates additional interfacial interactions in the soft/hard composite. The fracture of the ceramic skeleton exposes new bare surfaces that can interact more with the hydrogel matrix, providing extra mechanical recovery in the soft/hard composite material. To test this hypothesis, we conducted multiple loading-unloading cyclic tests with varying waiting times. As a representative sample, we used the soft/hard composites fabricated from the S1 skeleton with 4 M AAc and either 0.01 mol% or 0.1 mol% MBAA (referred to the AAc concentration) (**Fig. 7**). The reason for preparing two samples with different cross-linker

concentrations is that the hydrogel with a lower cross-linker concentration possesses more flexible polymer chains, making it easier to adapt to the bare surface of the ceramic skeleton during the waiting time and thus providing a higher healing ability.

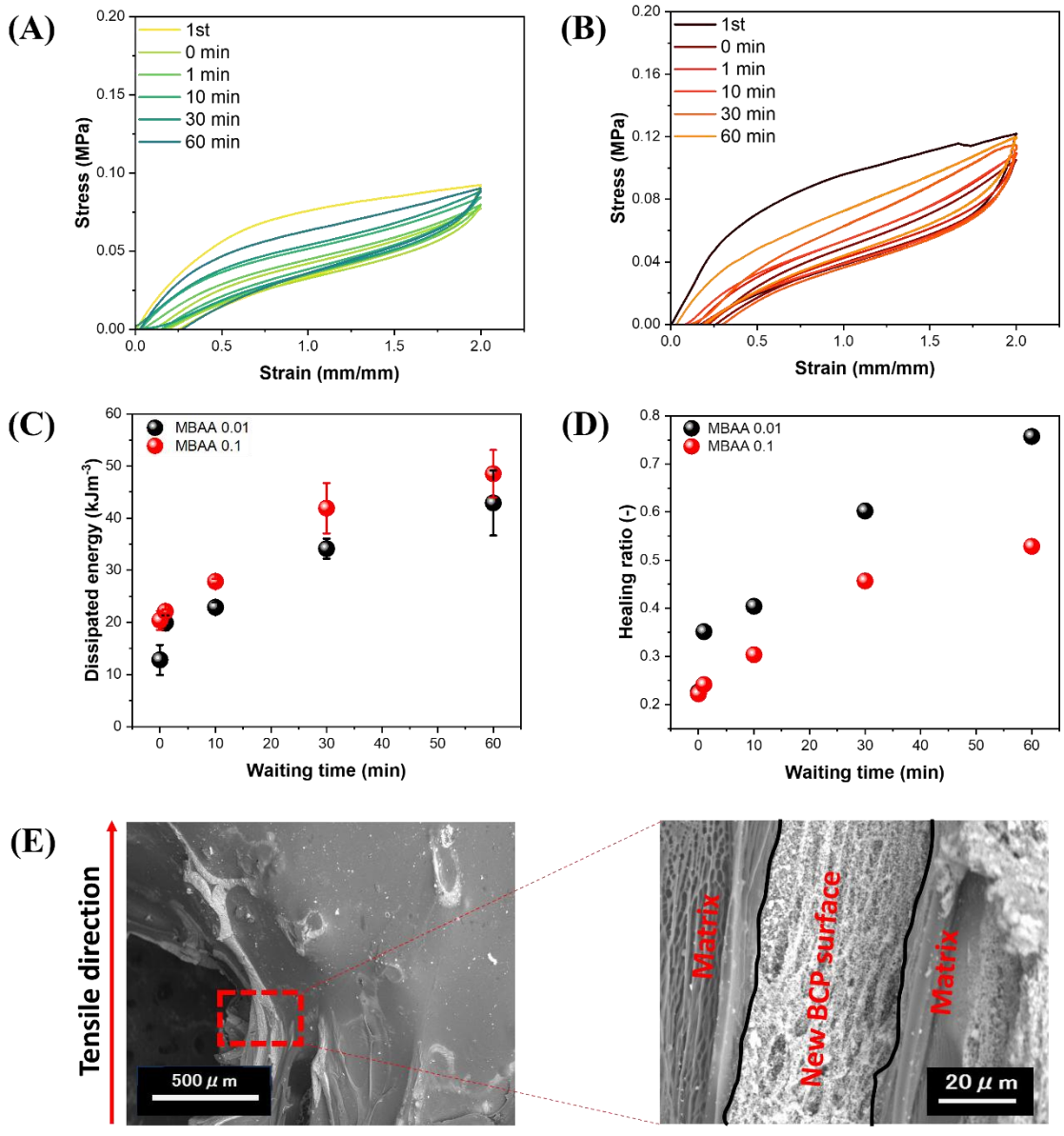

Fig. 7 Loading-unloading cyclic tests to evaluate the healing ratio of PAAc-S1 soft/hard composite with different waiting times after the first cycle. (A) with 0.01 mol% MBAA. (B) with 0.1 mol% MBAA. (C) Dissipated energy calculated from the hysteresis area. (D) Healing ratio calculated from hysteresis of the first cycle over that of second cycle. (E) Generation of new BCP surface area after the tensile deformation as revealed by SEM observation.

According to the results in **Fig. 7**, the hysteresis area for both PAAc0.01-S1 and PAAc0.1-S1 increased after the first cycle with longer waiting times. The PAAc0.1-S1 composite exhibited higher dissipated energy than the PAAc0.01-S1 composite, indicating that the more densely cross-linked network requires more energy to deform [34]. This denser network enables the material to withstand higher forces and dissipate energy more effectively. Conversely, in terms of the healing ratio, PAAc0.01-S1 demonstrated greater healing, reaching approximately 76% after 1 hour of waiting time, while PAAc0.1-S1 achieved only about 53% at the same waiting time. The incomplete recovery (less than 100% healing) is attributed to micro-damage in the PAAc hydrogel matrix, primarily caused by the breaking of covalent cross-linkers during deformation. Additionally, during the first loading-unloading cycle, the dissipated energy is dominated by the fracture of the skeleton, debonding of the matrix from the ceramic skeleton, and the breaking of Ca-mediated ionic bonds within the matrix.

Under cyclic loading-unloading tests, the fracture of the ceramic skeleton exposes new bare surfaces (**Fig. 7E**). It is possible that these new surfaces further interact with the hydrogel matrix through calcium-mediated ionic bonds formed during the waiting period, a process controlled by the dual buffer effect. During this period, the recovery of physical bonds between the polymer matrix and the ceramic skeleton, as well as between the polymers themselves, occurs relatively quickly due to molecular-scale diffusion. However, the formation of additional interactions between the new bare surface of the skeleton and the polymer matrix exhibits slower dynamics because micrometer-scale diffusion is required. Additionally, the higher the crosslink density of the polymer matrix, the more constrained the polymer chains become, which restricts large-scale diffusion. As shown in **Fig. 7D**, the healing ratio were higher for the 0.01 mol% composite than for the 0.1 mol% composite, even later in the waiting period. This

suggests that flexible polymer chains with low crosslink density form interactions with the new bare interface through thermal motion.

3-3 Tuning the mechanical properties of soft/hard composite by using small pore skeleton

The size and structure of the pores in the ceramic skeleton significantly affect the mechanical properties of soft/hard composites. In this study, two distinct ceramic skeletons, S1 and S2, incorporated into a PAAc hydrogel matrix, were compared. The ceramic skeletons exhibit different architectural characteristics, including pore size, strut length, and quantity. As previously stated, the S1 skeleton displayed larger pore sizes, longer strut lengths, and fewer struts compared to the S2 skeleton. We hypothesize that the soft/hard composite containing the S2 skeleton will exhibit superior mechanical properties due to the improved architecture of S2. This enhanced architecture reduces local stress concentrations, thereby increasing the overall mechanical properties of the structure. To assess the influence of pore structure on the mechanical properties, uniaxial tensile tests and loading-unloading tests, as depicted in **Fig. 8**, were conducted on the soft/hard composites.

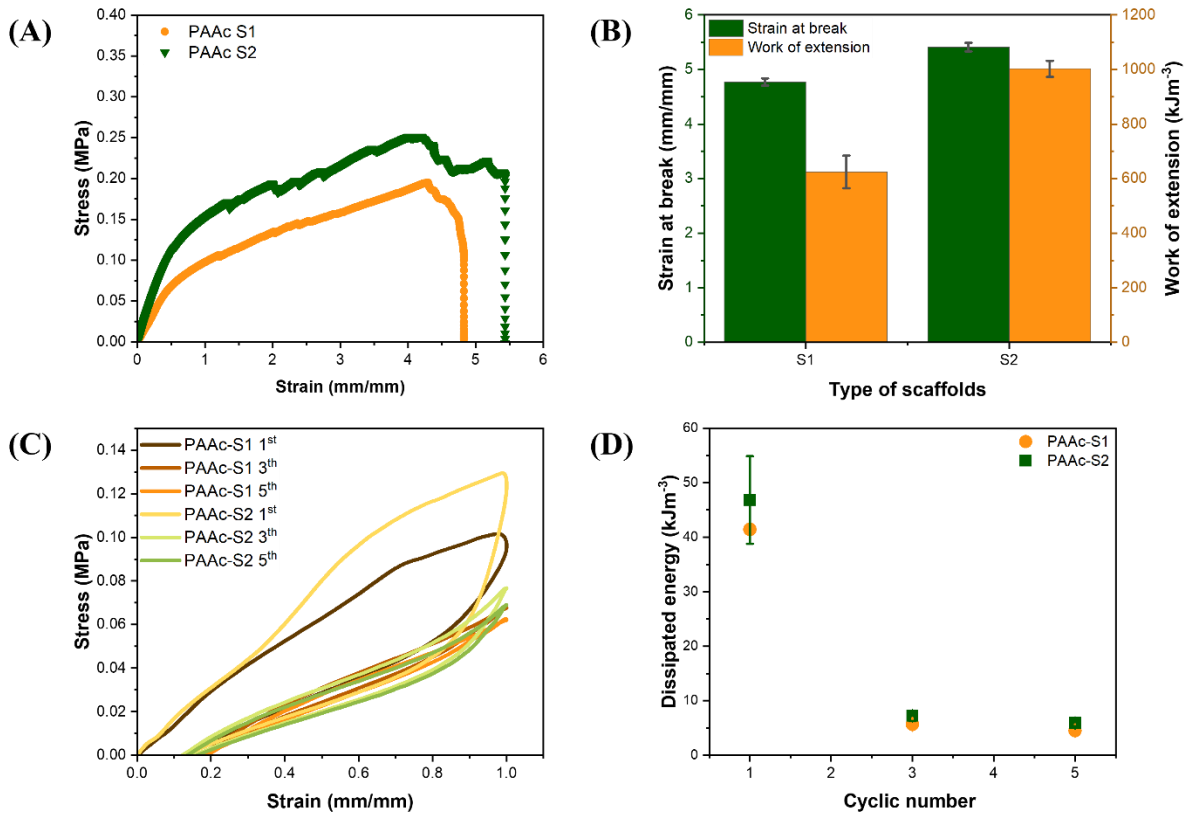

Fig. 8 (A) Tensile profile of soft/hard composite with different type of skeletons. (B) Strain at break and work of extension of PAAc-S1 and PAAc S2 composites. (C) Loading-unloading uniaxial tensile profiles up to 5th cycles. (D) Dissipated energy of soft/hard composite with different type of skeletons under loading-unloading uniaxial tensile test.

Remarkably, the combination of the S2 skeleton and hydrogel matrix demonstrated superior performance in terms of strain at break and work of extension (5.4 mm/mm, 1002 kJ/m^3) compared to the PAAc-S1 soft/hard composite (4.8 mm/mm, 625 kJ/m^3). The S2 skeleton, with its smaller pore size and shorter strut lengths, results in a greater interfacial area for interactions between the ceramic and the PAAc hydrogel matrix. This robust interfacial adhesion facilitates the effective transmission of force between the flexible hydrogel matrix and the hard ceramic reinforcement phase under mechanical loading. Additionally, the S2 skeleton enables a more homogeneous distribution and penetration of the ceramic reinforcement phase

throughout the hydrogel matrix. This consistent load distribution in the composite material ensures efficient force transfer and even stress distribution, resulting in higher fracture strain. In contrast, the larger pores and longer strut lengths of the S1 skeleton may lead to localized stress concentration and early structural failure.

To further analyze the effect of pore size on the mechanical properties of the soft/hard composites, we evaluated the durability of the composites with different types of ceramic skeletons through loading-unloading cyclic tests up to a strain of 1.0 mm/mm without waiting time between cycles (**Fig. 8C**). The PAAc-S2 soft/hard composite exhibited higher hysteresis areas compared to the PAAc-S1 composite. During the first cycle, significant damage occurs in the composite material, such as fracture of the ceramic skeleton and debonding of the matrix from the skeleton. This initial damage leads to a high dissipation of energy. In subsequent cycles, the damage may stabilize, meaning that while some further damage might occur, the overall dissipation mechanism becomes more predictable and stabilizes. This could result in relatively constant dissipated energy from cycle to cycle after the initial cycle. Furthermore, after the first cycle, the stress distribution within the composite might become more uniform. The redistribution of stress occurs due to changes in microstructural features, such as crack paths and the contact area between the matrix and skeleton. This redistribution can also lead to the stabilization of dissipated energy as the material adjusts to the cyclic loading conditions.

To further validate the influence of distinct porous structures on the mechanical properties, we investigated the skeleton mass ratio in the soft/hard composite material using TGA (**Fig. S9**). TGA analysis revealed that the skeleton mass ratio was 31wt% for the PAAc0.1-S2 soft/hard composite, which is higher than the 28wt% skeleton mass ratio for the PAAc0.1-S1 composite. This suggests that the soft/hard composite with the S2 skeleton, characterized by a smaller pore structure, provides a higher surface area that interacts more

effectively with the PAAc hydrogel matrix, as supported by SEM analysis. Consequently, the increased surface area of the S2 skeleton in the soft/hard composite likely leads to enhanced interactions between the HAp and β-TCP present in the skeleton and the PAAc hydrogel, contributing to the excellent mechanical properties observed in the PAAc-S2 composite.

However, TGA analysis indicates that both PAAc-S1 and PAAc-S2 soft/hard composite materials contain a significant amount of water, approximately 50 wt%, as evidenced by the substantial weight loss observed below 500 °C [35]. This high-water content, compared to natural bone, which has around 15-25% water by volume [36], contributes to the weaker mechanical properties of these composites. However, the primary reason for their much lower strength compared to bone is the absence of the fine hierarchical structure that is characteristic of natural bone.

4. Conclusion

The fabrication of the novel soft/hard composite presented in this work demonstrates the successful application of the sacrificial bond concept. By combining a porous ceramic skeleton with a hydrogel matrix in a single thermal polymerization process, the resulting composite effectively mimics the molecular interactions and hierarchical structure of natural bone, incorporating multiple sacrificial structures. The brittle porous ceramic skeleton serves as the primary sacrificial bond, while the hydrogel matrix prevents fatal and global fractures. Additionally, the interactions between the skeleton and matrix, as well as between the released calcium ions and the hydrogel, contribute to the overall toughening mechanisms. Moreover, the fracture of the brittle ceramic skeleton can expose new surface areas, facilitating further interactions with the hydrogel and providing an additional recovery pathway.

This combination allows the composite to replicate key features of bone, including its hierarchical organization and the interplay between hard and soft components. This work presents a simple yet effective strategy for fabricating soft/hard composites that mimic the structure and properties of natural bone. The ability to combine a porous ceramic skeleton and a hydrogel matrix in a single step opens up new possibilities for developing advanced biomaterials and tissue engineering applications. The unique sacrificial and multiscale structure of the composite can lead to enhanced mechanical performance and improved integration with biological systems, paving the way for further exploration and applications in regenerative medicine and beyond.

Acknowledgements

This research was supported by the Japan Society for the Promotion of Science (JSPS) KAKENHI (grant number JP22H04968, JP22K21342, JP23K21134) and Japan Science and Technology Agency (JST) FOREST (grant number JPMJFR201Q). The first author acknowledges the Ministry of Education, Culture, Sports, Science and Technology (MEXT) for the scholarship during his doctoral program.

Conflict of interest

There is no conflict of interest to declare.

References

[1] Boskey, A. L. (2007, December 1). Mineralization of Bones and Teeth. *Elements*, *3*(6), 385–391. https://doi.org/10.2113/gselements.3.6.385.

[2] Robey, P. G. (1996, January). Vertebrate Mineralized Matrix Proteins: Structure and Function. *Connective Tissue Research*, *35*(1–4), 131–136. https://doi.org/10.3109/03008209609029183.

[3] Fantner, G. E.; Adams, J.; Turner, P.; Thurner, P. J.; Fisher, L. W.; Hansma, P. K. Nanoscale Ion Mediated Networks in Bone: Osteopontin Can Repeatedly Dissipate Large Amounts of Energy. Nano Lett. 2007, 7 (8), 2491−2498. https://doi.org/10.1021/nl0712769.

[4] Cavelier, S.; Dastjerdi, A. K.; McKee, M. D.; Barthelat, F. Bone Toughness at the Molecular Scale: A Model for Fracture Toughness Using Crosslinked Osteopontin on Synthetic and Biogenic Mineral Substrates. Bone 2018, 110, 304−311. https://doi.org/10.1016/j.bone.2018.02.022.

[5] Fantner, G. E.; Hassenkam, T.; Kindt, J. H.; Weaver, J. C.; Birkedal, H.; Pechenik, L.; Cutroni, J. A.; Cidade, G. A. G.; Stucky, G. D.; Morse, D. E.; Hansma, P. K. Sacrificial Bonds and Hidden Length Dissipate Energy as Mineralized Fibrils Separate during Bone Fracture. Nat. Mater. 2005, 4 (8), 612−616. https://doi.org/10.1038/nmat1428.

[6] Kashimura, N., Suzuki, Y., Nonoyama, T., & Gong, J. P. (2024). Tough Hydroxyapatite Hydrogels Based on Bone-like Self-Regulatory Sacrificial Bond Formation. *Chemistry of Materials*, *36*(6), 2944–2952. https://doi.org/10.1021/acs.chemmater.3c03272.

[7] Oftadeh, R., Perez-Viloria, M., Villa-Camacho, J. C., Vaziri, A., & Nazarian, A. (2015). Biomechanics and Mechanobiology of Trabecular Bone: A Review. *Journal of Biomechanical Engineering*, *137*(1). https://doi.org/10.1115/1.4029176.

[8] Kozielski, M., Buchwald, T., Szybowicz, M., Błaszczak, Z., Piotrowski, A., & Ciesielczyk, B. (2011). Determination of composition and structure of spongy bone tissue in human head of femur by Raman spectral mapping. *Journal of Materials Science: Materials in Medicine*, *22*(7), 1653–1661. https://doi.org/10.1007/s10856-011-4353-0.

[9] Favus MJ. Primer on the metabolic bone diseases and disorders of metabolism. 4th ed. Philadelphia: Lippincott Williams & Wilkins; 1999.

[10] Hart, N.H.; Nimphius, S.; Rantalainen, T.; Ireland, A.; Siafarikas, A.; Newton, R.U. Mechanical basis of bone strength: Influence of bone material, bone structure and muscle action. J. Musculoskelet. Neuronal Interact. 2017, 17, 114. [PubMed]

[11] Morgan, E. F., Unnikrisnan, G. U., & Hussein, A. I. (2018). Bone Mechanical Properties in Healthy and Diseased States. *Annual Review of Biomedical Engineering*, *20*(1), 119–143. https://doi.org/10.1146/annurev-bioeng-062117-121139.

[12] Niu, Y., Du, T., & Liu, Y. (2023). Biomechanical Characteristics and Analysis Approaches of Bone and Bone Substitute Materials. *Journal of Functional Biomaterials*, *14*(4), 212. https://doi.org/10.3390/jfb14040212.

631 [13] Jun, I. K., Koh, Y. H., Song, J. H., Lee, S. H., & Kim, H. E. (2006). Improved compressive
632 strength of reticulated porous zirconia using carbon coated polymeric sponge as novel
633 template. *Materials Letters*, *60*(20), 2507–2510. https://doi.org/10.1016/j.matlet.2006.01.031.

634 [14] Wen, Z. H., Han, Y. S., Liang, L., & Li, J. B. (2008). Preparation of porous ceramics with
635 controllable pore sizes in an easy and low-cost way. *Materials Characterization*, *59*(9), 1335–
636 1338. https://doi.org/10.1016/j.matchar.2007.11.010.

637 [15] Sung, J. H., Shin, K. H., Koh, Y. H., Choi, W. Y., Jin, Y., & Kim, H. E. (2011). Preparation
638 of the reticulated hydroxyapatite ceramics using carbon-coated polymeric sponge with
639 elongated pores as a novel template. *Ceramics International*, *37*(7), 2591–2596.
640 https://doi.org/10.1016/j.ceramint.2011.04.023.

641 [16] Gong, J. P. (2010). Why are double network hydrogels so tough? *Soft Matter*, *6*(12), 2583.
642 https://doi.org/10.1039/b924290b.

643 [17] Gong, J., Katsuyama, Y., Kurokawa, T., & Osada, Y. (2003, July 17). Double-Network
644 Hydrogels with Extremely High Mechanical Strength. *Advanced Materials*, *15*(14), 1155–1158.
645 https://doi.org/10.1002/adma.200304907.

646 [18] Gregor, A., Filová, E., Novák, M., Kronek, J., Chlup, H., Buzgo, M., Blahnová, V.,
647 Lukášová, V., Bartoš, M., Nečas, A., & Hošek, J. (2017). Designing of PLA scaffolds for bone
648 tissue replacement fabricated by ordinary commercial 3D printer. *Journal of Biological*
649 *Engineering*, *11*(1). https://doi.org/10.1186/s13036-017-0074-3.
650
651 [19] Wu, Z., Sun, L., Tian, Z., Wang, J., Li, J., & Hu, Z. (2014). Preparation and properties of
652 reticulated porous γ-Y2Si2O7 ceramics with high porosity and relatively high
653 strength. *Ceramics International*, *40*(7), 10013–10020.
654 https://doi.org/10.1016/j.ceramint.2014.02.100.
655
656 [20] Li, Y., Xiao, Y., & Liu, C. (2017). The Horizon of Materiobiology: A Perspective on
657 Material-Guided Cell Behaviors and Tissue Engineering. *Chemical Reviews*, *117*(5), 4376–
658 4421. https://doi.org/10.1021/acs.chemrev.6b00654.
659
660
661 [21] Stella, S. M., Sridhar, T. M., Ramprasath, R., Gimbun, J., & Vijayalakshmi, U. (2022).
662 Physio-Chemical and Biological Characterization of Novel HPC
663 (Hydroxypropylcellulose):HAP (Hydroxyapatite):PLA (Poly Lactic Acid) Electrospun
664 Nanofibers as Implantable Material for Bone Regenerative Application. *Polymers*, *15*(1), 155.
665 https://doi.org/10.3390/polym15010155.
666
667
668 [22] Skorokhod, V. V., Solonin, S. M., Dubok, V. A., Kolomiets, L. L., Permyakova, T. V., &
669 Shinkaruk, A. V. (2010). Decomposition activation of hydroxyapatite in contact with β-
670 tricalcium phosphate. *Powder Metallurgy and Metal Ceramics*, *49*(5–6), 324–329.
671 https://doi.org/10.1007/s11106-010-9239-z.
672

673 [23] Baldassarre, F., Altomare, A., Corriero, N., Mesto, E., Lacalamita, M., Bruno, G., . . . Siliqi,
674 D. (2020). Crystal Chemistry and Luminescence Properties of Eu-Doped Polycrystalline
675 Hydroxyapatite Synthesized by Chemical Precipitation at Room Temperature. *Crystals*, *10*(4),
676 250. https://doi.org/10.3390/cryst10040250.
677
678
679 [24] Zhang, Y., Ai, J., Wang, D., Hong, Z., Li, W., & Yokogawa, Y. (2013). Dissolution
680 properties of different compositions of biphasic calcium phosphate bimodal porous ceramics
681 following immersion in simulated body fluid solution. *Ceramics International*, *39*(6), 6751–
682 6762. https://doi.org/10.1016/j.ceramint.2013.02.004.
683
684 [25] Katti, K. S., Turlapati, P., Verma, D., Bhowmik, R., Gujjula, P. K., & Katti, D. R. (2006b).
685 Static and Dynamic Mechanical Behavior of Hydroxyapatite-Polyacrylic Acid Composites
686 Under Simulated Body Fluid. *American Journal of Biochemistry & Biotechnology/American*
687 *Journal of Biochemistry and Biotechnology*, *2*(2), 73–79.
688 https://doi.org/10.3844/ajbbsp.2006.73.79.

689 [26] Verma, D., Bhowmik, R., Mohanty, B., Katti, D. R., & Katti, K. S. (2005). Role of
690 Interfacial Interactions on Mechanical Properties of Biomimetic Composites for Bone Tissue
691 Engineering. *MRS Proceedings*, *898*. https://doi.org/10.1557/proc-0898-l08-03.

692 [27] Bohner, M. (2000). Calcium orthophosphates in medicine: from ceramics to calcium
693 phosphate cements. *Injury*, *31*, D37–D47. https://doi.org/10.1016/s0020-1383(00)80022-4.

694 [28] Margolis, H. C., & Moreno, E. C. (1992). Kinetics of hydroxyapatite dissolution in acetic,
695 lactic, and phosphoric acid solutions. *Calcified Tissue International*, *50*(2), 137–143.
696 https://doi.org/10.1007/bf00298791.
697
698 [29] Zhang, S., Wang, X., Yang, J., Chen, H., & Jiang, X. (2023). Micromechanical interlocking
699 structure at the filler/resin interface for dental composites: a review. *International Journal of*
700 *Oral Science*, *15*(1). https://doi.org/10.1038/s41368-023-00226-3.
701
702 [30] Chen, Y., Zheng, Y., Zhou, Y., Zhang, W., Li, W., She, W., . . . Miao, C. (2023). Multi-
703 layered cement-hydrogel composite with high toughness, low thermal conductivity, and self-
704 healing capability. *Nature Communications*, *14*(1). https://doi.org/10.1038/s41467-023-39235-
705 5.
706
707 [31] Pukánszky, B. (1990). Influence of interface interaction on the ultimate tensile properties
708 of polymer composites. *Composites*, *21*(3), 255–262. https://doi.org/10.1016/0010-
709 4361(90)90240-w.

710 [32] Cao, C., & Li, Y. (2020, January 8). Highly stretchable calcium ion/polyacrylic acid
711 hydrogel prepared by freezing-thawing. *Journal of Materials Science*, *55*(12), 5340–5348.
712 https://doi.org/10.1007/s10853-019-04332-8.

[33] Nap, R. J., & Szleifer, I. (2018, October 28). Effect of calcium ions on the interactions between surfaces end-grafted with weak polyelectrolytes. *The Journal of Chemical Physics*, *149*(16), 163309. https://doi.org/10.1063/1.5029377.

[34] Abdallah, M., Martin, M., El Tahchi, M. R., Balme, S., Faour, W. H., Varga, B., . . . Bechelany, M. (2019). Influence of Hydrolyzed Polyacrylamide Hydrogel Stiffness on Podocyte Morphology, Phenotype, and Mechanical Properties. *ACS Applied Materials & Interfaces*, *11*(36), 32623–32632. https://doi.org/10.1021/acsami.9b09337.

[35] Li, Z., Su, Y., Xie, B., Wang, H., Wen, T., He, C., . . . Wang, D. (2013). A tough hydrogel–hydroxyapatite bone-like composite fabricated in situ by the electrophoresis approach. *Journal of Materials Chemistry B*, *1*(12), 1755. https://doi.org/10.1039/c3tb00246b.

[36] Boskey, A. L., & Robey, P. G. (2013). The Composition of Bone. *Primer on the Metabolic Bone Diseases and Disorders of Mineral Metabolism*, 49–58. https://doi.org/10.1002/9781118453926.ch6.